IEEE Access
Multidisciplinary | Rapid Review | Open Access Journal

Received February 14, 2020, accepted March 3, 2020, date of publication March 13, 2020, date of current version October 22, 2020.

Digital Object Identifier 10.1109/ACCESS.2020.2980796

Modeling and Dynamic Response Analysis of a Compound Power-Split Hybrid Electric Vehicle During the Engine Starting Process

YANZHAO SU[1], LING SU[2], MINGHUI HU[1], (Member, IEEE), DATONG QIN[1], (Member, IEEE), CHUNYUN FU[1], (Member, IEEE), AND HAISHENG YU[3]

[1]State Key Laboratory of Mechanical Transmissions, Chongqing University, Chongqing 400044, China
[2]Chongqing Changan Automobile Company Ltd., Chongqing 401120, China
[3]Corun CHS Technology Company Ltd., Shanghai 201501, China

Corresponding author: Minghui Hu (minghui_h@163.com)

This work was supported in part by the National Natural Science Foundation of the People's Republic of China under Grant 51675062, in part by the National Key Research and Development Program of China under Grant 2018YFB0106104, and in part by the Fundamental Research Funds for the Central Universities under Grant 2018CDJDCD0001.

ABSTRACT This study is aimed at revealing the dynamic response characteristics of a power-split hybrid electric vehicle (HEV) during the mode transition process with the engine starting. In this paper, for a hybrid powertrain system whose engine is directly connected to a compound power-split transmission, the equivalent lever method is first used to analyze the mode transition process with the engine starting. Then, based on the theoretical formulations and lookup tables, a dynamic model of the compound power-split HEV is established in detail, taking into consideration the engine ripple torque, battery-motor characteristics, dynamic meshing force between gears, and shaft spring-damping characteristics. The powertrain dynamic model is verified by a bench test. Moreover, taking the vehicle jerk and engine starting time as the evaluation indexes of the dynamic response characteristics, the influencing factors of the dynamic response characteristics in the engine starting process are analyzed comprehensively from the aspects of the engine, battery-motor, and engine starting condition. Finally, the engine starting process is synthetically optimized based on the obtained impact law of different influencing factors. The simulation results show that the synthesis optimization method can effectively reduce vehicle jerks and the engine starting time and improve driving comfort during the engine starting process.

INDEX TERMS Dynamic response characteristics, engine starting, powertrain modeling, hybrid electric vehicle (HEV), power-split transmission.

I. INTRODUCTION

Since a hybrid electric vehicle (HEV) combines an internal combustion engine, electric drive system, and energy storage device, it has better fuel economy and lower emissions when choosing different working modes than traditional cars [1]–[5]. However, as the hybrid powertrain system adds an electric power source, the vehicle powertrain structure becomes more complicated and the complexity of the vehicle control system is increased. Moreover, owing to the significant differences in the transient torque response characteristics of the engine and the motor, the limitations of the battery charge and discharge power, and the limitations of the motor external characteristics, the output torque of the powertrain system may exhibit sudden changes or fluctuations [6]–[10]. Such transients will worsen driving comfort and reduce the service life of the powertrain system. Therefore, it is necessary to investigate the influencing factors of the dynamic response characteristics to improve driving comfort during the mode transition process, especially when this involves the engine starting process.

Some scholars have examined the dynamic response characteristics of the mode transition process for hybrid electric vehicles. Tong [11] and Du *et al.* [12] found that the powertrain system exhibits obvious shocks when the target torques of the engine and the motor change significantly or suddenly. Based on an established parallel HEV, Hong *et al.* [13] found that the closing and opening process of the engine clutch

The associate editor coordinating the review of this manuscript and approving it for publication was Jianyong Yao.

causes changes in the vehicle speed response and the vibration of the vehicle transmission system. Zhang *et al.* [14] and Hu *et al.* [15] analyzed the mechanism of the vehicle jerk produced in the mode transition process according to the dynamic expression of the vehicle jerk, and found that the torque change rate of the powertrain system has a significant impact on the vehicle jerk. Canova *et al.* [16]–[18] established a model of the engine pulsating torque and found that the maximum overshoot and response delay of the engine speed were the main factors of vibrations during engine starting. These studies mainly focused on the dynamic characteristics in the mode transition process for a parallel HEV with a clutch between the engine and the transmission, and did not take into account the influence of the battery-motor characteristics and the engine starting condition points.

For the Toyota hybrid system (THS), Yoshioka [19], Komada and Yoshioka [20], Yoshioka *et al.* [21], and Kawabata *et al.* [22] found that the pump pressure in the cylinder is the main factor of engine vibration during the engine starting process, and the engine mount also causes vibration in the transmission system. Kuang [23], Hwang [24], and Chen and Hwang [25] established a model of the engine pulsating torque and found that the main causes of system vibrations during engine starting are engine pressure in the engine cylinder and the engine start initial angle. Tang *et al.* [26]–[28] established a vehicle dynamics model including the engine pulsating torque, engine mounting system, transmission system, suspension system, and vehicle body, and analyzed the resonance characteristics of a power-split HEV in the processes of engine starting and stopping. Zeng *et al.* [29]–[30] established a power-split HEV model including an engine model based on a BP neural network, and found that the torque change rate of the power source is the main reason for large vehicle jerk during the mode switching process. Using experimental data from a power-split HEV, Liu *et al.*[31]–[32] found that the longitudinal vibration of the seat track was most affected by the engine initial angle during the engine starting process. Wang *et al.* [33] tested vehicle jerks in the mode transition process with engine starting, and found that the main reason for the obvious jerk was the engine ripple torque. Although these studies focused on the dynamic characteristics of a power-split HEV, they ignored the limitations of the battery-motor dynamic characteristics and the influence of the engine starting condition points.

To sum up, the current research studies on the dynamic response characteristics of the mode transition process mainly focused on the effects of the torque change rate, engine ripple torque, engine starting initial angle, and engine speed overshoot on the jerks and vibrations of the powertrain system. However, the influence of the engine cooling water temperature, engine intake manifold pressure, engine intake valve close timing, and engine demand angular acceleration on the dynamic response characteristics of the powertrain system were not considered. In addition, the effects of the battery-motor dynamic characteristics and engine starting condition points on the dynamic response characteristics of the powertrain system during the engine starting process have not yet been considered.

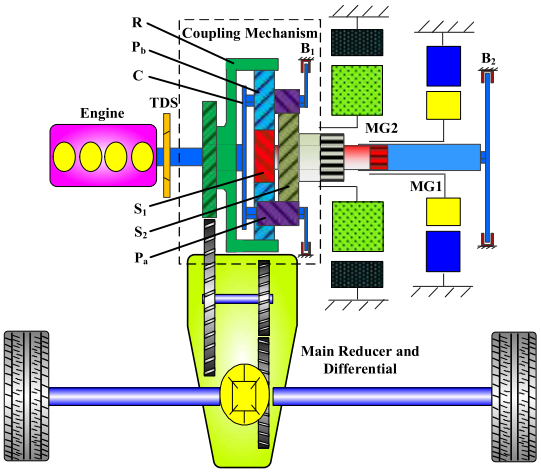

FIGURE 1. Structural diagram of compound power-split HEV.

Therefore, different from the existing research, for a power-split HEV whose engine is directly connected to a compound power-split transmission, this paper comprehensively reveals the dynamic response characteristics during the mode transition process with the engine starting. There are three main contributions in this paper: 1) Based on the theoretical formulations and lookup tables, a dynamic model of a compound power-split HEV is established in detail, and the HEV model is verified by a bench test. 2) Taking the vehicle jerk and engine starting time as the evaluation indexes of the dynamic response characteristics, the influencing factors and law of dynamic response characteristics in the engine starting process are analyzed comprehensively from the aspects of the engine, battery-motor, and engine starting conditions points. 3) To improve driving comfort, the engine starting process is synthetically optimized based on the obtained impact law of different influencing factors.

The remaining sections of this study are organized as follows. The mode transition process with engine starting is analyzed in Section II. Then, a power-split HEV model is established and verified by bench experiments in Section III. In Section IV, the evaluation indexes of the dynamic response characteristics are defined. Based on the defined evaluation indexes, the influencing factors of the dynamic response characteristics in the engine starting process are analyzed in Section V. Further, the engine starting process is synthetically optimized based on the obtained impact law in Section VI. Finally, concluding remarks are provided in Section VII.

II. MODE TRANSITION PROCESS ANALYSIS WITH ENGINE STARTING

As shown in Fig. 1, a compound power-split HEV with two motors and a Ravigneaux planetary gear train is the subject of research in this paper. The small motor (MG1) is directly connected to small sun S_1, which can be locked by brake B_2. The large motor (MG2) is directly connected to big sun S_2. The engine is directly connected to carrier C through a

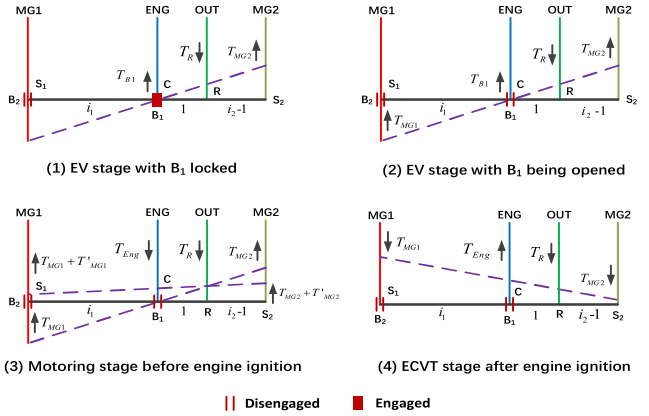

FIGURE 2. Equivalent lever diagram from EV mode to ECVT mode.

torsional damper spring (TDS), which can be locked by brake B_1. P_a represents the rear planetary gear, and P_b represents the front planetary gear. Ring R is the power output, which is connected to the main reducer of the HEV.

Fig. 2 shows the equivalent lever diagram in the mode transition process from electric vehicle (EV) mode to electric continuous variable transmission (ECVT) mode. In this process, the four stages are as follows: (1) EV stage with B_1 locked, (2) EV stage with B_1 being opened, (3) motoring stage before engine ignition, and (4) ECVT stage after engine ignition.

(1) In stage 1, B_1 is locked, and MG2 torque T_{MG2} will overcome ring load torque T_R to drive the vehicle. (2) In stage 2, B_1 is quickly opened by the hydraulic system. MG1 torque T_{MG1} and MG2 torque T_{MG2} will keep the engine still and drive the vehicle at the same time. (3) In stage 3, B_1 has been fully opened. Based on the original T_{MG1}, MG1 superimposes T'_{MG1} to drag the engine to the engine ignition speed. In order to eliminate the influence of the MG1 engine start process on the ring output, based on the original T_{MG2}, MG2 provides a superimposed compensation torque T'_{MG2} to keep the vehicle driving normally. (4) In the last stage, when the engine preset speed is reached, the engine starts ignition, and engine torque T_{Eng} and the two motors' torques drive the vehicle together.

Since the engine starting process mainly occurs in the third and fourth working stages after brake B_1 is fully opened, the dynamic characteristics in the third and fourth working stages will be mainly analyzed in this paper. According to the equivalent lever method [34], the dynamic expressions of the MG1 and MG2 torques, Eq. (1), can be obtained in the third and fourth working stages.

$$\begin{cases} T_{MG1} = \dfrac{(i_2-1)\,T_{r\_req} + i_2\left(T_{Eng} - \left(I_{Eng}+I_C\right)\ddot{\theta}_{\text{Eng\_des}}\right)}{i_1 - i_2} \\ \quad + \left(I_{s_1} + I_{MG1}\right)\left(i_0 i_1 \ddot{\theta}_{WH} + (1-i_1)\,\ddot{\theta}_{\text{Eng\_des}}\right) \\ T_{MG2} = \dfrac{(i_1-1)\,T_{r\_req} + i_1\left(T_{Eng} - \left(I_{Eng}+I_C\right)\ddot{\theta}_{\text{Eng\_des}}\right)}{i_2 - i_1} \\ \quad + \left(I_{s_2} + I_{MG2}\right)\left(i_0 i_2 \ddot{\theta}_{WH} + (1-i_2)\,\ddot{\theta}_{\text{Eng\_des}}\right) \end{cases} \tag{1}$$

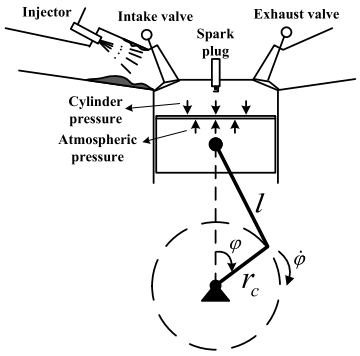

FIGURE 3. Schematic of single-cylinder engine operation.

where T_{MG1} is the MG1 torque, T_{MG2} is the MG2 torque, T_{r_req} is the required torque at the ring gear, T_{Eng} is the desired engine torque, I_{MG1} and I_{MG2} are the MG1 inertia and MG2 inertia, and I_{S1} and I_{S2} are the inertias of the small and large sun gear, respectively. $\ddot{\theta}_{WH}$ is the wheel angular acceleration. I_{Eng} is the engine inertia, I_C is the carrier inertia, and $\ddot{\theta}_{\text{Eng\_des}}$ is the engine demand angular acceleration. i_0 is the final drive ratio, and i_1 and i_2 are the planetary parameters of the front and rear rows, respectively.

The "S-curve" function $f\ (x, a, b, c)$ from Eq. (2) is taken as the engine demand angular acceleration $\ddot{\theta}_{\text{Eng\_des}}$. The S-curve function $f\ (x, a, b, c)$ is defined as follows:

$$\ddot{\theta}_{\text{Eng\_des}} = f\ (x, a, b, c) = \frac{1}{1 + e^{-a(x-c)}} \cdot b \tag{2}$$

where a can change the change rate of $\ddot{\theta}_{\text{Eng\_des}}$, b can change the maximum value of $\ddot{\theta}_{\text{Eng\_des}}$, and c can move along the time axis.

III. POWERTRAIN DYNAMIC MODELING

Based on the theoretical formulations and lookup tables, a dynamic model of the HEV is established using MATLAB/Simulink software. The compound power-split HEV model includes a dynamic engine model, a TDS model, battery-motor dynamic model, compound power-split coupling mechanism model, brake model, and vehicle longitudinal dynamic model.

A. DYNAMIC ENGINE MODEL

Fig. 3 shows a schematic of the single-cylinder operation of the engine, which includes a fuel injector, spark plug, intake and exhaust, and mechanical movement part. In this paper, the dynamic engine model includes two main parts: the in-cylinder thermodynamic model and the engine ripple torque (ERT) model. The main purpose of the in-cylinder thermodynamic model is to provide the cylinder pressure for the ERT model. In the dynamic engine model, the main experimental data from the engine manufacturer include the engine cooling water temperature, intake temperature, intake manifold pressure, exhaust pressure, and friction torque.

1) IN-CYLINDER THERMODYNAMIC MODEL

For the thermodynamic system shown in Fig. 3, the general equations for the working process of the internal combustion engine can be obtained by applying the first law of thermodynamics. The gas pressure $P_{cyl,i}(\varphi)$ in the i-th cylinder ($i = 1, 2, 3, 4$) is obtained as follows [35], [36]:

$$\begin{cases} \dfrac{dT_{temp}}{d\varphi} = \dfrac{1}{m\frac{\partial u}{\partial T_{temp}}}\left(\dfrac{dQ_B}{d\varphi} + \dfrac{dQ_w}{d\varphi} - P_{cyl,i}(\varphi)\right. \\ \quad \dfrac{dV_{cyl}}{d\varphi} + \dfrac{dm_{s_c}}{d\varphi}h_{s_c} \\ \quad \left. + \dfrac{dm_e}{d\varphi}h_e - u\dfrac{dm}{d\varphi} - m\dfrac{\partial u}{\partial \lambda}\dfrac{d\lambda}{d\varphi}\right) \\ \dfrac{dm}{d\varphi} = \dfrac{dm_{\mathrm{B}}}{d\varphi} + \dfrac{dm_{\mathrm{s_c}}}{d\varphi} + \dfrac{dm_{\mathrm{e}}}{d\varphi} \\ P_{cyl,i}(\varphi)\, V_{cyl}(\varphi) = m(\varphi)\, RT_{temp}(\varphi) \end{cases} \tag{3}$$

Here,

$$V_{cyl}(\varphi) = \frac{V_s}{2}\left(\frac{2}{\varepsilon_c - 1} + 1 - \cos\varphi + \frac{1}{\lambda_s}\left(1 - \sqrt{1 - \lambda_s^2 \sin^2\varphi}\right)\right) \tag{4}$$

where T_{temp}, φ, m, u, V_{cyl}, λ, R, V_s, ε_c, and λ_s are the cylinder temperature, crank angle, gas mass, specific thermodynamic energy, instantaneous working volume, instantaneous excess air coefficient, gas constant, geometric working volume, geometric compression ratio, and crank connection ratio, respectively. Q is the exchange heat with gas, and h is the specific enthalpy. Subscript s_c represents the gas that flows into the cylinder through the intake valve, subscript e denotes the gas that flows out through the exhaust valve, subscript B stands for the heat release term of fuel combustion, and subscript w represents the exchange of heat through the wall and out of the system. $\lambda_s = r_c/l$, where r_c is the crankshaft radius, and l is the connection rod length.

2) ENGINE RIPPLE TORQUE MODEL

For a four-stroke engine, the engine total torque T_{ERT} before the engine flywheel is equal to the superposition of each cylinder torque with a 180° difference [6], [7].

$$T_{ERT} = \sum_i T_{cyl,i} = \sum_i \left(T_{P_i} + T_{I_i}\right) + T_F \tag{5}$$

where $T_{cyl,i}$ is the ERT in the i-th cylinder ($i = 1, 2, 3, 4$), T_{P_i} is the cylinder pressure ripple torque of the engine, in which the cylinder pressure is obtained by $P_{cyl,i}(\varphi)$ from the in-cylinder thermodynamic model. T_{I_i} is the inertia torque of the piston and connecting rod, and T_F is the piston and air valve friction torque obtained by the engine test.

As illustrated in Fig. 4, the ERT of the motoring stage is plotted at different engine speeds when the throttle position is 6%. We find that the ERT fluctuates once every 180° periodically in a 720° cycle and that the ERT curves present significant periodic fluctuations. This means that the engine characteristics from the engine steady-state map cannot completely reflect the actual engine dynamic characteristics.

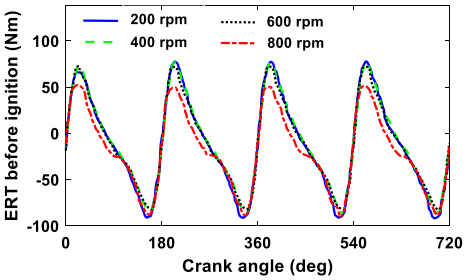

FIGURE 4. Engine ripple torque.

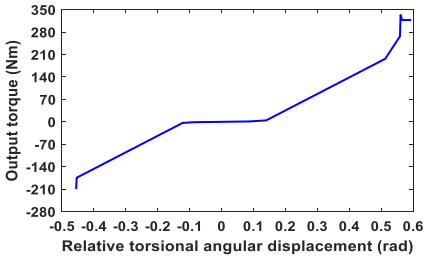

FIGURE 5. Characteristic curve of torsional stiffness.

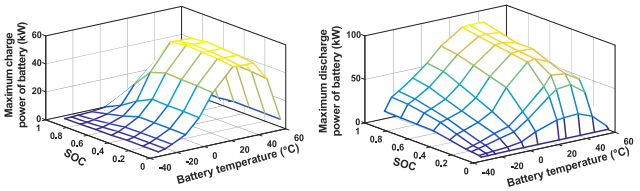

FIGURE 6. Maximum charge and discharge power of battery.

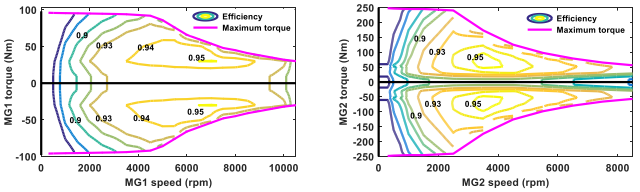

FIGURE 7. Speed-torque characteristics and efficiencies of two motors.

B. TORSIONAL DAMPER SPRING MODEL

Based on the characteristic curve of torsional stiffness (shown in Fig. 5) and the hysteretic damping torque of the torsional damper, a TDS model is established using MATLAB/Simulink as a lookup table.

C. BATTERY–MOTOR DYNAMIC MODEL

A battery-motor dynamic model is established by considering the influence of the battery state of charge (SOC) and temperature on the battery charge and discharge power in Fig. 6, the speed-torque characteristics of the two motors, and the energy conversion efficiency between the battery and motors in Fig. 7. In this model, the battery is the power supply and provides the voltage and current for the motor. The internal

resistance model of the battery is established to reflect the dynamic characteristics of the battery.

The general equation of an internal resistance model of the battery is expressed as follows [4], [37]:

$$U_b = E_b - I_b R_b \tag{6}$$

where U_b is the battery bus voltage, E_b is the battery electromotive force, I_b is the battery current, and R_b is the internal resistance of the battery.

A three-phase permanent magnet synchronous motor with sinusoidal back electromotive force is built in the rotor reference frame (q-d frame). The basic motor electromagnetic torque T_{MG} is obtained as follows [7], [37]:

$$T_{MG} = 1.5\, p_{\mathrm{s}} \left[\lambda_a i_q + (L_d - L_q) i_d i_q\right] \tag{7}$$

where p_{s} is the number of pole pairs; λ_a is the amplitude of the flux induced by the permanent magnets of the rotor in the stator phases; L_q and L_d are the q-axis and d-axis inductances, respectively; and i_q and i_d are the q-axis and d-axis currents, respectively.

D. COMPOUND POWER-SPLIT COUPLING MECHANISM MODEL

Considering the dynamic meshing force between gears, a torsional planetary dynamic model is built using the lumped-parameter method [6], [7], [38]. The motion equations of the torsional planetary dynamic model are expressed as follows:

$$I_{\mathrm{s}_1}\ddot{\theta}_{\mathrm{s}_1} = T_{s_1} + \sum_{n=1}^{N} F_{ys_1b_n} \cdot \mathrm{r}_{s_1} \tag{8}$$

$$I_{s_2}\ddot{\theta}_{s_2} = T_{s_2} + \sum_{n=1}^{N} F_{ys_2a_n} \cdot \mathrm{r}_{s_2} \tag{9}$$

$$\begin{aligned} I_{\mathrm{ce}}\ddot{\theta}_C = {} & T_C + \sum_{n=1}^{N} F_{ys_2a_n} \cdot \cos\alpha_{s_2} \cdot \mathrm{r}_C \\ & + \sum_{n=1}^{N} F_{ys_1b_n} \cdot \cos\alpha_{s_1} \cdot \mathrm{r}_C - \sum_{n=1}^{N} F_{yRb_n} \cdot \cos\alpha_R \cdot \mathrm{r}_C \end{aligned} \tag{10}$$

$$I_R\ddot{\theta}_R = \sum_{n=1}^{N} F_{yRb_n} \cdot \mathrm{r}_R - T_{TI} \tag{11}$$

$$I_a\ddot{\theta}_{a_nc} = F_{ya_nb_n} \cdot r_a - F_{ys_2a_n} \cdot r_a \tag{12}$$

$$I_{\mathrm{b}}\ddot{\theta}_{b_nc} = F_{ya_nb_n} \cdot r_{\mathrm{b}} - F_{yRb_n} \cdot r_b - F_{ys_1b_n} \cdot r_b \tag{13}$$

where I, r, α, $\ddot{\theta}$ and T are the inertia, base circle radius, meshing angle, angular acceleration, and external torque corresponding to specific subscriptions, respectively. $F_{ys_1b_n}$ is the dynamic engagement force between S_1 and P_{b}, $F_{ys_2a_n}$ is the dynamic engagement force between S_2 and P_{a}, $F_{ys_2a_n}$ is the dynamic engagement force between R and P_{b}, and $F_{ya_nb_n}$ is the dynamic engagement force between P_a and P_b. These dynamic engagement forces are given in [38]. T_{TI} is the actual load torque at the TI shaft. Note that TI is an elastic shaft equivalent to the ring for the tire and half shaft in Fig. 25. a and b are subscriptions of the planetary gears of the rear row and front row, respectively. $N(n)$ is the planet number, and $I_{ce} = I_c + NI_a + NI_b$.

E. BRAKE MODEL

A brake model is established to reflect the dynamic characteristics of the brake system. The model includes three states: disengagement, sliding, and engagement [7]. The transmitted torque T_B of the brake is expressed as follows:

$$T_B = \begin{cases} 0, & \textit{disengagement} \\ \mu_{sl} r_B (P_B - P_0) \\ \quad A_B N_B sgn(\dot{\theta}_{c\_g}), & \textit{sliding} \\ [-\mu_{st} r_B (P_B - P_0) \\ \quad A_B N_B \mu_{st} r_B (P_B - P_0) A_B N_B], & \textit{engagement} \end{cases} \tag{14}$$

where $\dot{\theta}_{c\_g}$ is the carrier speed, μ_{sl} and μ_{st} are the sliding and static friction coefficients of the friction plate, respectively. r_B is the effective friction radius, P_B is the brake oil pressure, P_0 is the prefill pressure, A_B is the equivalent friction area, and N_B is the number of friction surfaces.

F. VEHICLE LONGITUDINAL DYNAMIC MODEL

Considering the spring-damping characteristics of the tire and half shaft, the vehicle longitudinal dynamic model is formulated as

$$\dot{T}_{TI} = k_{TI}\left(\dot{\theta}_R - \dot{\theta}_L\right) + C_{TI}\left(\ddot{\theta}_R - \ddot{\theta}_L\right) \tag{15}$$

$$\begin{cases} m_v \dot{V}_x = T_{TI} i_0 / r_v - T_f / r_v \\ T_f = r_v (0.5 C_d \rho A V_x^2 \mathrm{sgn}\,(V_x) + \\ \quad m_v g f \cos\beta + m_v g \sin\beta) \end{cases} \tag{16}$$

where k_{TI} and C_{TI} are the equivalent stiffness and damping of the tire and half shaft at the TI shaft in Fig. 25, respectively. $\dot{\theta}_R$ and $\ddot{\theta}_R$ are the speed and angular acceleration at the ring, and $\dot{\theta}_L$ and $\ddot{\theta}_L$ are the speed and angular acceleration of point B in Fig. 25, respectively. m_v is the vehicle equivalent mass, i_0 is the final drive ratio, r_v is the tire radius, V_x is the longitudinal vehicle speed, T_f is the load torque at the wheel, g is the gravitational acceleration, f is the tire rolling resistance coefficient, β is the ramp angle, C_d is the air resistance coefficient, ρ is the air density, and A is the vehicle frontal area.

G. POWERTRAIN MODEL VALIDATION

A compound power-split HEV model is established by integrating the above component models using MATLAB/Simulink. As shown in Fig. 8, a powertrain test bench for the power-split HEV is built to validate the effectiveness of the powertrain model. In the test, the dynamometer speed is set at 27 rad/s, and the required torque at the ring gear is set at 30 Nm. Then, the mode transition process with engine starting is tested. The input variables of the powertrain model are from the experimental data obtained in the test. They include the engine cooling water temperature, battery

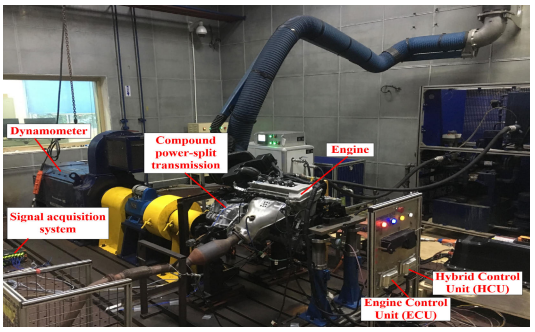

FIGURE 8. Powertrain dynamic model validation.

TABLE 1. Main parameters of compound power-split HEV.

Parameters	Values
Engine maximum torque/speed (Nm/rpm)	145/3600
MG1/MG2 maximum torque (Nm)	96/246
Planetary parameter of front row i_1	-3.179
Planetary parameter of rear row i_2	2.342
Final drive ratio i_0	4.044
Carrier inertia I_C (kg·m^2)	0.0039
Ring inertia I_R (kg·m^2)	0.0017
Inertia ($I_{MG1} + I_{S1}$) of MG1 and S_1 (kg·m^2)	0.041
Inertia ($I_{MG2} + I_{S2}$) of MG2 and S_2 (kg·m^2)	0.0723
Engine inertia I_{Eng} (kg·m^2)	0.18
Vehicle equivalent mass m_v (kg)	1538
Wheel radius r_v (m)	0.31
Vehicle frontal area A (m^2)	2.19
Air resistance coefficient C_d	0.307
Tire rolling resistance coefficient	0.0137
Equivalent TI torsional stiffness k_{TI} (Nm·rad^{-1})	2864
Equivalent TI torsional damping c_{TI} (Nm·s·rad^{-1})	15

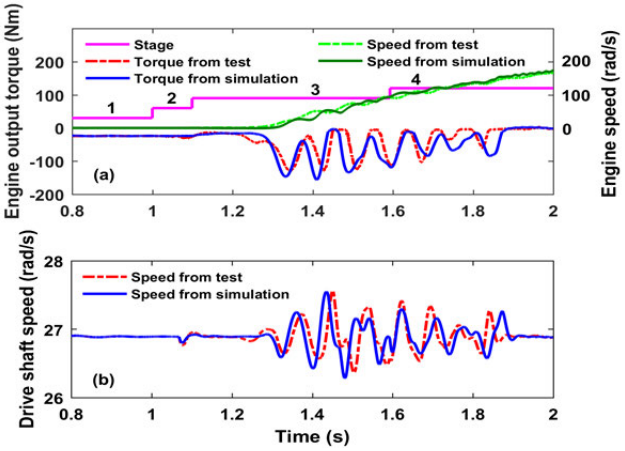

FIGURE 9. Powertrain dynamic model validation.

SOC, engine demand angular acceleration, and engine ignition speed. In this paper, many parameters and coefficients used for modeling are provided by the manufacturers. The main parameters of the power-split HEV are listed in Table 1.

As shown in Fig. 9(a), in the third and fourth stages, the torque of the engine output shaft presents obvious torque fluctuation, and the engine speed presents low frequency and large amplitude fluctuation. As seen in Fig. 9(b), the speed of the drive shaft also fluctuates obviously, which may cause the shock and oscillation of the transmission system. Moreover, it can be seen from Fig. 9(a) and Fig. 9(b) that in the mode transition process with engine starting, the change trend of the torque and speed of the engine output shaft and drive shaft speed obtained by simulation is basically consistent with the corresponding results obtained by the bench test. By comparing the simulation results and test results, it can be seen that the powertrain plant model can effectively and accurately reflect the dynamic characteristics of the powertrain system during the mode transition process with engine starting.

IV. EVALUATION INDEXES OF DYNAMIC RESPONSE CHARACTERISTICS

As the vehicle jerk (especially the maximum absolute value of the vehicle jerk) is synchronous with human feeling and is not affected by the road bumps or driver operation, it can better reflect the dynamic characteristics of the vehicle [39]. In addition, the longer the engine starting time, the longer the time of the shock and vibration in the engine starting process. Therefore, the vehicle jerk, maximum absolute value of the vehicle jerk, and engine starting time will be used as the objective evaluation indexes of the dynamic response characteristics in the mode transition process with the engine starting in order to study the influencing factors of driving comfort and the corresponding dynamic coordinated control methods.

The vehicle jerk j is the derivative of the vehicle longitudinal acceleration or the second derivative of the vehicle longitudinal speed, and its expression is as follows:

$$j = \frac{da_v}{dt} = \ddot{V}_x \tag{17}$$

where a_v is the vehicle longitudinal acceleration.

The maximum absolute value of vehicle jerk $j_{a-\max}$ is defined as

$$j_{a-\max} = \max(|j|) \tag{18}$$

The engine starting time t_{start} is expressed as

$$t_{start} = t_f - t_0 \tag{19}$$

where t_0 is the start time of the starting engine, and t_f is the end time of the starting engine.

V. ANALYSIS OF INFLUENCING FACTORS ON DYNAMIC RESPONSE CHARACTERISTICS

Based on the evaluation indexes of the dynamic response characteristics, the basic control (BC) method based on Eq. (1) is used to analyze the influencing factors of the dynamic response characteristics of the engine starting process from the aspects of the engine, battery-motor, and engine starting condition points. This lays a theoretical foundation for the corresponding dynamic coordinated control method in the mode transition process with engine starting. Table 2 lists the basic simulation parameters of the engine starting process.

TABLE 2. Basic parameters of model simulation.

Parameters	Values
Engine starting condition point	Point C in Fig. 10
Engine cooling water temperature (°C)	25
Ratio coefficient of ERT	1
Engine initial crankshaft angle (°)	95
Engine intake manifold pressure (kPa)	101
Engine intake valve close timing (°)	50
Engine demand angular acceleration (rad/s^2)	$a = 100$, $b = 400$, $c = 0.193$
Battery charging power limitation (kW)	52.3
Battery discharging power limitation (kW)	78.8
Battery temperature (°C)	30
Battery SOC (%)	35
Maximum torque ratio of two motors	1
Motor torque change rate limitation	without
Motor torque compensation control	without

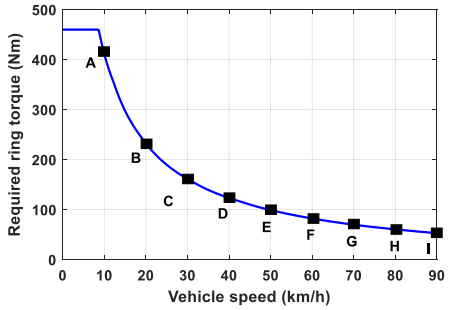

FIGURE 10. Engine starting condition points.

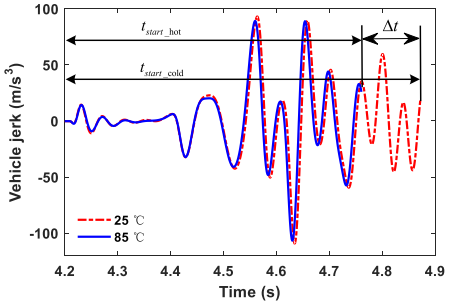

FIGURE 11. Vehicle jerks under cold and hot conditions.

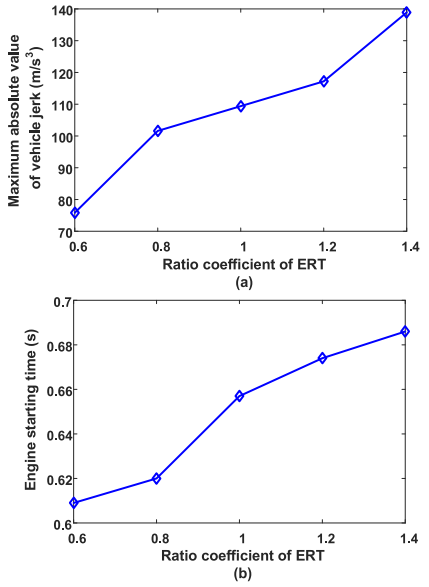

FIGURE 12. Effects of ratio coefficient of ERT on maximum absolute value of vehicle jerk and engine starting time.

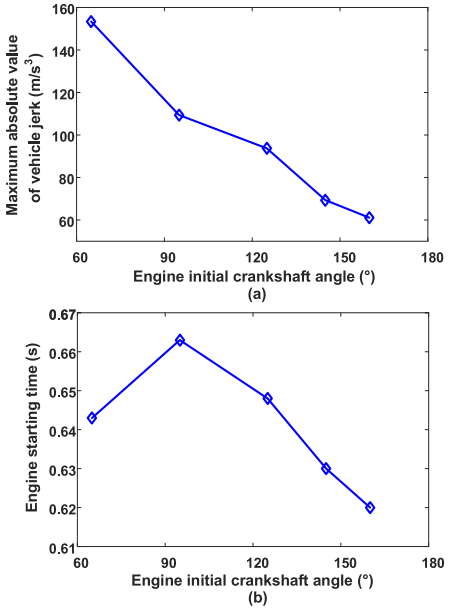

FIGURE 13. Effects of ICA on maximum absolute value of vehicle jerk and engine starting time.

A. EFFECT OF ENGINE ON DYNAMIC RESPONSE CHARACTERISTICS

1) EFFECT OF ENGINE COOLING WATER TEMPERATURE

Using the basic simulation parameters of the engine starting process in Tables 1 and 2, the engine starting process is simulated under the following conditions of the cooling water temperature: 25 °C (cold start) and 85 °C (hot start). Fig. 11 shows the vehicle jerks during cold and hot engine starting. It can be seen from this figure that $j_{a-\max}$ in the process of an engine cold start is 109.4 m/s^3, and $j_{a-\max}$ in the process of an engine hot start is 106.8 m/s^3. This shows that the vehicle jerk of a cold start and hot start does not change significantly.

In addition, the engine cold starting time t_{start_cold} is 0.663 s, the engine hot starting time t_{start_hot} is 0.552 s, and the engine cold starting time is 0.111 s longer than the engine hot starting time. This is mainly because the engine ignition speed is higher during a cold start than a hot start, and the engine friction torque increases with a decrease in the engine cooling water temperature. Therefore, the time when the engine speed reaches the ignition speed during the cold start is longer than that during the hot start.

2) EFFECT OF ENGINE RIPPLE TORQUE

Using the basic simulation parameters of the engine starting process in Tables 1 and 2, the engine ripple torque

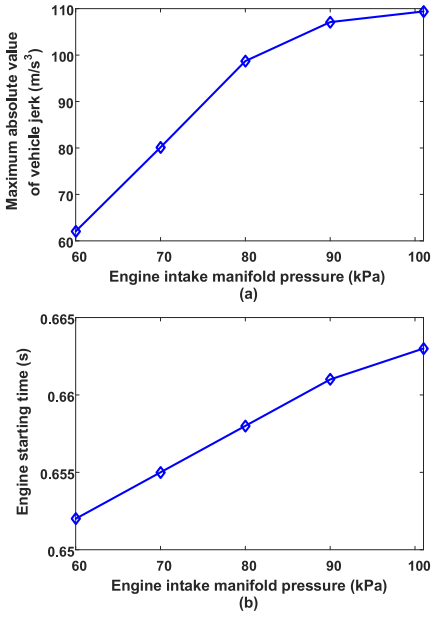

FIGURE 14. Effects of engine intake manifold pressure on maximum absolute value of vehicle jerk and engine starting time.

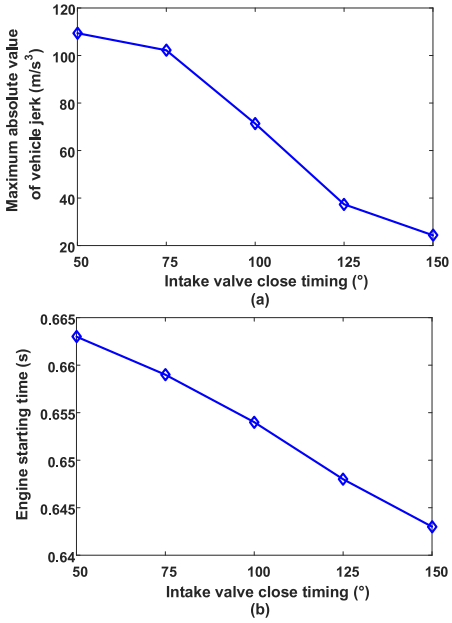

FIGURE 15. Effects of IVCT on maximum absolute value of vehicle jerk and engine starting time.

(ERT) shown in Fig. 4 is multiplied by the ratio coefficient to analyze the effect of the ERT on the dynamic response characteristics of the powertrain system. It can be seen from Fig. 12 that when the ratio coefficient of the ERT increases from 0.6 to 1.4, $j_{a-\max}$ increases from 75.83 m/s^3 to 138.9 m/s^3 and the engine starting time increases from 0.609 s to 0.686 s. This shows that $j_{a-\max}$ and the engine starting time increase correspondingly with an increase in the ratio coefficient of the ERT. This also shows that the factors that can cause an engine ripple torque change will also affect the dynamic response characteristics of the powertrain system.

3) EFFECT OF ENGINE INITIAL CRANKSHAFT ANGLE

The engine initial crankshaft angle (ICA) is the angle between the position of the first cylinder piston and the bottom dead center. The effects of different engine ICAs on $j_{a-\max}$ and the engine starting time are simulated under the basic simulation parameters of the engine starting process in Tables 1 and 2. It can be seen from Fig. 13(a) that when the engine ICA increases from 65° to 160°, $j_{a-\max}$ decreases from 153.4 m/s^3 to 61.1 m/s^3, and $j_{a-\max}$ decreases by 92.3 m/s^3. It can be observed from Fig. 13(b) that the engine starting time increases first and then decreases, and the difference between the maximum and minimum values is only 0.043 s. This shows that the influence of the engine ICA on the engine starting time is not obvious. By contrast, the ICA has a more obvious impact on the vehicle jerk. Because the stop position of the engine piston directly determines the engine ICA, controlling the stop position of the engine piston in the proper range to reduce the vibrations of the engine starting process has become a hot research topic [40].

4) EFFECT OF ENGINE INTAKE MANIFOLD PRESSURE

The effects of the engine intake manifold pressure on $j_{a-\max}$ and the engine starting time are simulated under the basic simulation parameters of the engine starting process in Tables 1 and 2. As shown in Fig. 14(a), when the engine intake manifold pressure increases from 60 kPa to 101 kPa (ambient atmospheric pressure), $j_{a-\max}$ increases from 62.06 m/s^3 to 109.4 m/s^3, and $j_{a-\max}$ increases by 47.34 m/s^3. It can be seen from Fig. 14(b) that the engine starting time also shows a trend of increasing with an increase in the engine intake manifold pressure, but the difference between the maximum and minimum values is only 0.011 s, which is not obvious.

5) EFFECT OF ENGINE INTAKE VALVE CLOSE TIMING

The engine intake valve close timing (IVCT) is the angle between the engine piston position and the bottom dead center when the intake valve is closed. The effects of the engine IVCT on $j_{a-\max}$ and the engine starting time are simulated under the basic simulation parameters of the engine starting process in Tables 1 and 2. It can be seen from Fig. 15(a) that when the engine IVCT increases from 50° to 150°, $j_{a-\max}$ decreases from 109.4 m/s^3 to 24.32 m/s^3, and $j_{a-\max}$ decreases by 85.08 m/s^3. As shown in Fig. 15(b), the engine starting time also shows a tendency to decrease as the engine IVCT increases. However, the difference between the maximum value and minimum value is only 0.02 s and is not very obvious.

6) EFFECT OF ENGINE DEMAND ANGULAR ACCELERATION

The engine demand angular acceleration is defined as the "S-curve" function $f(x, a, b, c)$ from Eq. (2). The engine

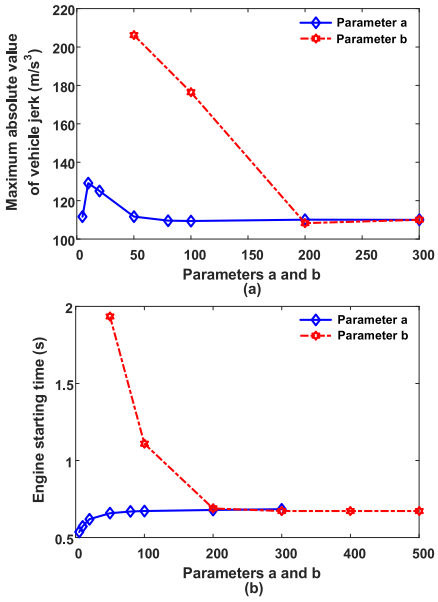

FIGURE 16. Effects of parameters a and b on maximum absolute value of vehicle jerk and engine starting time.

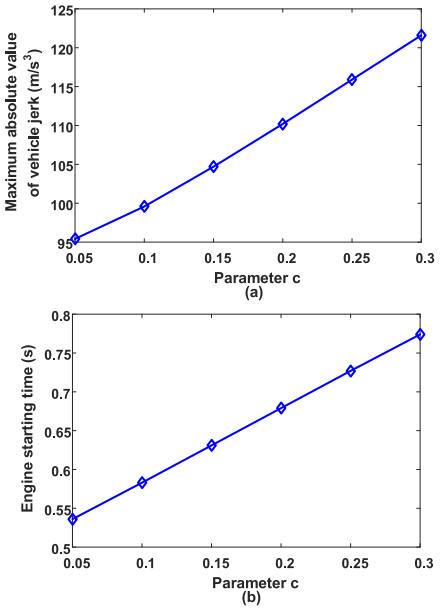

FIGURE 17. Effects of parameter c on the maximum absolute value of vehicle jerk and engine starting time.

demand angular acceleration is affected by three parameters *a, b,* and *c*. Therefore, the effects of parameters *a, b,* and *c* on $j_{a-\max}$ and the engine starting time are simulated under the basic simulation parameters of the engine starting process in Tables 1 and 2.

As can be seen from Fig. 16(a), when parameter *a* is between 5 and 100, the maximum $j_{a-\max}$ appears to be 129.1 m/s^3, and $j_{a-\max}$ gradually stabilizes at 109.4 m/s^3 after parameter *a* is greater than 100. When parameter *b* increases from 50 to 200, $j_{a-\max}$ decreases from 206.2 m/s^3 to 108.3 m/s^3, and then $j_{a-\max}$ stabilizes at 109.4 m/s^3 as parameter *b* increases. As shown in Fig. 16(b), the engine starting time increases as parameter *a* increases, and the engine starting time stabilizes at 0.663 s when parameter *a* is greater than 100. When parameter *b* increases from 50 to 200, the engine starting time is reduced from 1.934 s to 0.663 s, and then the engine starting time is basically stabilized at 0.663 s as parameter *b* increases. As seen in Fig. 17(a), $j_{a-\max}$ increases as parameter *c* increases. It can be seen from Fig. 17(b) that the engine starting time also increases as parameter *c* increases.

B. EFFECT OF BATTERY-MOTOR ON DYNAMIC RESPONSE CHARACTERISTICS

1) EFFECT OF BATTERY TEMPERATURE AND SOC

The effects of the battery temperature on $j_{a-\max}$ and the engine starting time are simulated under the basic simulation parameters of the engine starting process in Tables 1 and 2. It can be seen from Fig. 18(a) that $j_{a-\max}$ is 109.4 m/s^3 when the battery temperature is between 10 °C and 50 °C, and $j_{a-\max}$ increases significantly when the battery temperature is lower than 10 °C or higher than 50 °C. This is mainly because the battery temperature directly affects the charge and discharge power of the battery when the SOC value is given, which results in a limitation on the motor output torque. It can be seen from Fig. 18(b) that when the battery temperature is in the range of 0 °C to 55 °C, the engine starting time does not change significantly. However, when the battery temperature is −10 °C, the engine starting time increases significantly to 1.763 s. These data show that the low temperature of the battery at a given SOC will significantly affect the engine starting time.

The effects of the battery SOC on $j_{a-\max}$ and the engine starting time are simulated under the basic simulation parameters of the engine starting process in Tables 1 and 2. It can be seen from Fig. 19(a) that when the battery SOC is in the range of 15% to 85%, $j_{a-\max}$ is 109.4 m/s^3. When the battery SOC is less than 15% or greater than 85%, $j_{a-\max}$ increases significantly. From Fig. 19(b), it can be seen that the engine starting time is stable at 0.663 s when the battery SOC is in the range of 15% to 85%. The engine starting time decreases to 0.635 s when the SOC is 10% and increases to 0.741 s when the SOC is 90%. This is mainly because the battery SOC will directly affect the charge and discharge power of the battery when the battery temperature is given, which results in a limitation on the motor output torque.

2) EFFECT OF BATTERY CHARGE AND DISCHARGE POWER LIMITATIONS

The effects of battery power limitations on $j_{a-\max}$ and the engine starting time are simulated under the basic simulation parameters of the engine starting process in Tables 1 and 2. It can be seen from Fig. 20(a) that the maximum $j_{a-\max}$ reaches 138.4 m/s^3 when the battery discharge power

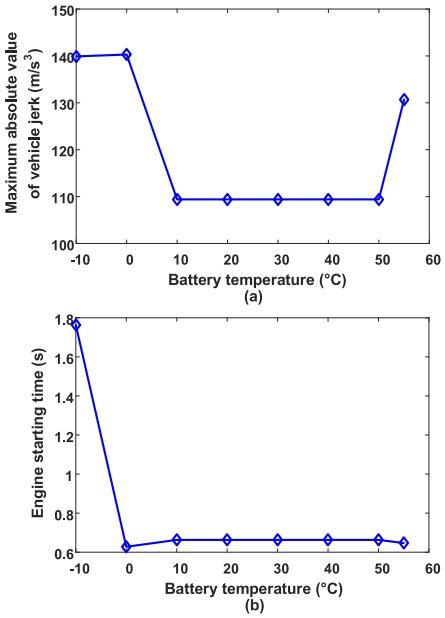

FIGURE 18. Effects of battery temperature on maximum absolute value of vehicle jerk and engine starting time.

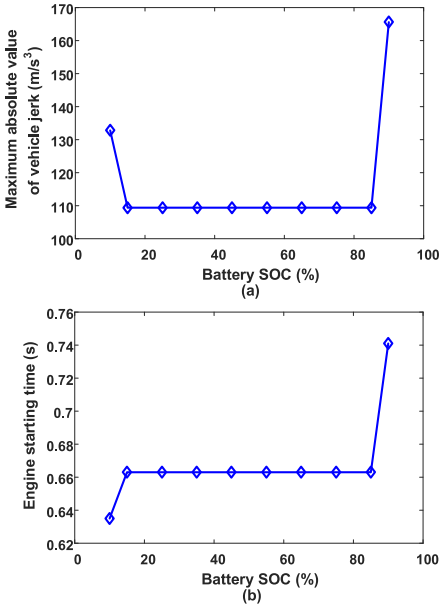

FIGURE 19. Effects of battery SOC on maximum absolute value of vehicle jerk and engine starting time.

is limited to 30 kW. When the battery discharge power limitation increases from 30 kW to 40 kW, $j_{a-\max}$ decreases from 138.4 m/s^3 to 109.4 m/s^3. Then, when the battery discharge power limitation is greater than 40 kW, $j_{a-\max}$ is stable at 109.4 m/s^3. It can be seen from Fig. 20(b) that when the discharge power limit is increased from 25 kW to 30 kW, the engine starting time is reduced from 0.72 s to 0.622 s. When the discharge power limit is increased from 30 kW to 40 kW, the engine starting time is increased from 0.622 s to

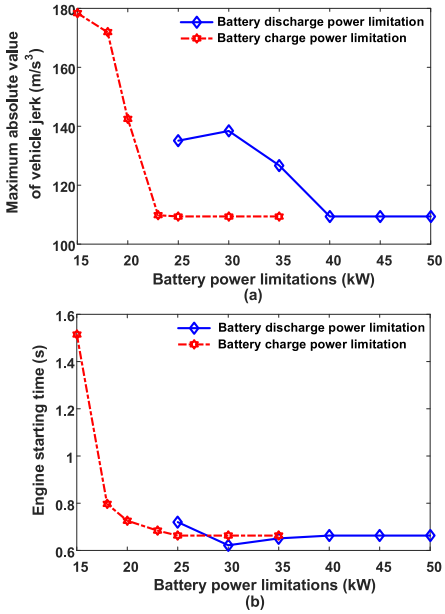

FIGURE 20. Effects of battery power limitations on maximum absolute value of vehicle jerk and engine starting time.

0.663 s. The engine starting time is still 0.663 s when the discharge power limit is greater than 40 kW. These data show that the vehicle jerk and engine starting time are no longer affected by the discharge power limit when the discharge power limit is greater than 40 kW.

As shown in Fig. 20(a), when the charging power limitation is increased from 15 kW to 25 kW, $j_{a-\max}$ is reduced from 178.4 m/s^3 to 109.8 m/s^3. With an increase in the battery charging power limit, $j_{a-\max}$ is stabilized at 109.4 m/s^3. It can be seen from Fig. 20(b) that when the charging power limit is increased from 15 kW to 25 kW, the engine starting time is reduced from 1.515 s to 0.663 s. When the charging power limit is greater than 25 kW, the starting time is maintained at 0.663 s. This shows that when the charging power limit is greater than 25 kW, the vehicle jerk and the engine starting time are no longer affected by the charging power limitation.

3) EFFECT OF MAXIMUM TORQUE RATIO OF TWO MOTORS

Based on the basic simulation parameters of the engine starting process in Tables 1 and 2, the maximum torque of the two motors is multiplied by the ratio coefficient to analyze the effects of the maximum torques of MG1 and MG2 on the dynamic response characteristics of the powertrain system. As shown in Fig. 21(a), when the maximum torque ratio of MG1 increases from 0.5 to 1.4, $j_{a-\max}$ decreases from 199.4 m/s^3 to 57.84 m/s^3. As can be seen from Fig. 21(b), the engine starting time first tends to decrease rapidly and then slowly decreases as the MG1 maximum torque ratio increases. From Fig. 21(a), it can be seen that when the maximum torque ratio of MG2 increases from 0.4 to 0.7, $j_{a-\max}$ rapidly decreases from 142.7 m/s^3 to 109.4 m/s^3. Then, when the maximum torque ratio of MG2 is greater than 0.7, $j_{a-\max}$

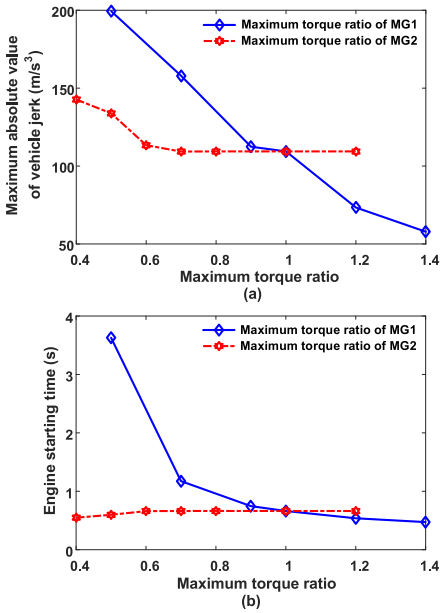

FIGURE 21. Effects of maximum torques of MG1 and MG2 on maximum absolute value of vehicle jerk and engine starting time.

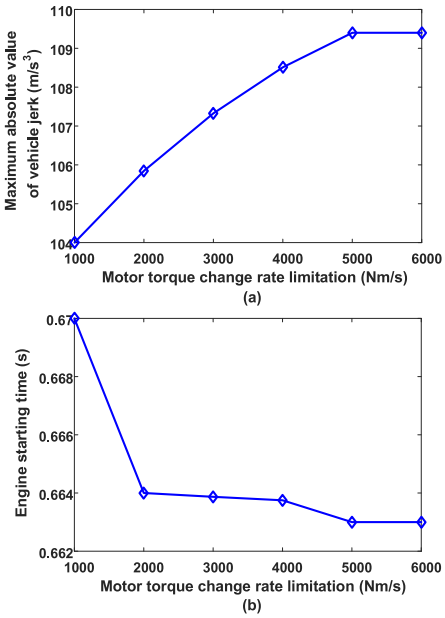

FIGURE 22. Effects of motor torque change rate on maximum absolute value of vehicle jerk and engine starting time.

is maintained at 109.4 m/s^3. It can be seen from Fig. 21(b) that when the maximum torque ratio of MG2 increases from 0.4 to 0.6, the engine starting time increases rapidly from 0.548 s to 0.661 s. Then, the engine starting time tends toward 0.663 s when the maximum torque ratio of MG2 is greater than 0.6.

4) EFFECT OF MOTOR TORQUE CHANGE RATE LIMITATION

The effects of motor torque change rate limitations on $j_{a-\max}$ and the engine starting time are simulated under the basic simulation parameters of the engine starting process in Tables 1 and 2. It can be seen from Fig. 22(a) that with an increase in the limitation of the motor torque change rate, $j_{a-\max}$ shows an increasing trend. When the change rate of the motor torque is greater than 5000 Nm/s, $j_{a-\max}$ is kept at 109.4 m/s^3. From Fig. 22(b), it can be seen that with an increase in the motor torque change rate limitation, the engine starting time shows a decreasing trend. When the change rate of the motor torque is higher than 5000 Nm/s, the engine starting time is basically stable.

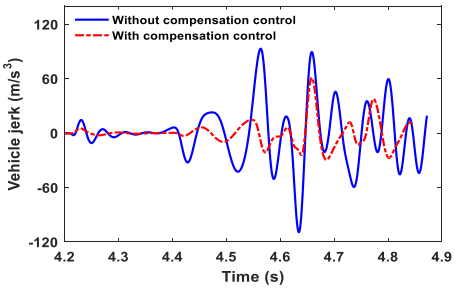

FIGURE 23. Effects of motor torque compensation control on vehicle jerk.

5) EFFECT OF MOTOR TORQUE COMPENSATION CONTROL

In the BC method from Eq. (1), the engine torque T_{Eng} required in the engine starting process is obtained by looking at the map of the engine resistance torque. Because the engine torque from a map is different from the actual ERT [6], the ERT cannot be compensated or offset by the torques of the two motors using the BC method. As a result, the ERT will directly transmit to the transmission system to worsen driving comfort and the reduce service life of the powertrain system. To address this problem, a motor torque compensation control based the engine torque estimation is used to start the engine. The actual engine torque is estimated by Eq. (20), which is obtained by the equivalent lever method [34]. Then, the estimated engine torque T_{Eng_est} is substituted for the engine torque T_{Eng} in Eq. (1) to obtain the distributed torques of the two motors. This can realize motor torque compensation control when starting the engine.

$$\begin{aligned} T_{Eng\_est} = {} & \frac{\left(I_{Eng}+I_C\right)\left(i_2\ddot{\theta}_{MG1}-i_1\ddot{\theta}_{MG2}\right)}{i_2-i_1}+[T_{MG1} \\ & -\left(I_{s_1}+I_{MG1}\right)\ddot{\theta}_{MG1}](i_1-1) \\ & +[T_{MG2}-\left(I_{s_2}+I_{MG2}\right)\ddot{\theta}_{MG2}](i_2-1) \end{aligned} \quad (20)$$

where $\ddot{\theta}_{MG1}$ and $\ddot{\theta}_{MG2}$ are the angular accelerations of MG1 and MG2, respectively.

The effects of motor torque compensation control on the vehicle jerk and engine starting time are simulated under the basic simulation parameters of the engine starting process in Tables 1 and 2. It can be seen from Fig. 23 that the motor torque compensation control reduces the engine starting time from 0.663 s to 0.636 s, but the range of reducing the engine starting time is not very large. However, the motor torque

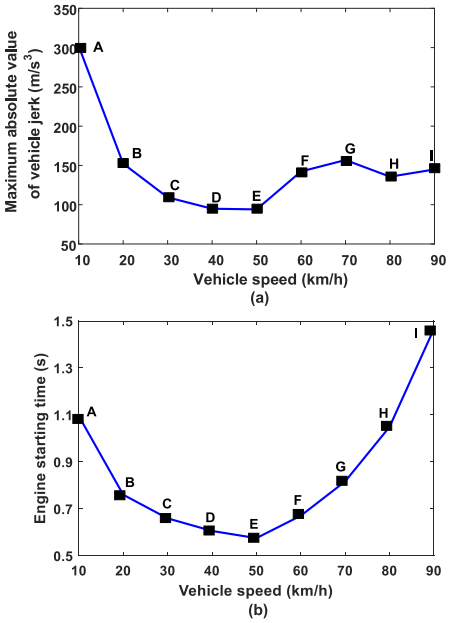

FIGURE 24. Effects of engine starting condition points on maximum absolute value of vehicle jerk and engine starting time.

compensation control significantly reduces the vehicle jerk, and reduces the $j_{a-\max}$ from 109.4 m/s^3 to 61.05 m/s^3.

C. EFFECT OF ENGINE STARTING CONDITION POINTS ON DYNAMIC RESPONSE CHARACTERISTICS

The effects of the engine starting condition points in Fig. 9 on the vehicle jerk and engine starting time are simulated under the basic simulation parameters of engine starting process in Tables 1 and 2. As can be seen from Fig. 24(a), $j_{a-\max}$ from point A to point I shows a trend of first decreasing and then increasing. Among them, $j_{a-\max}$ at point A reaches a maximum value of 302 m/s^3, and $j_{a-\max}$ at point E is the minimum value of 94.04 m/s^3. It is shown that the engine starting point under low-speed and heavy-load conditions has the largest impact on the vehicle jerk, and the engine starting point under medium-speed and medium-load conditions has the smallest impact on the vehicle jerk.

Although the load of engine starting decreases with an increase in the vehicle speed, the maximum torques of the two motors decrease as the speeds of the two motors increase. This will cause the motors to have insufficient torques to start the engine and compensate for fluctuating torques, thereby causing increases in the shocks and vibrations of the powertrain system. As shown in Fig. 24(b), the engine starting time from point A to point I also shows a trend of first decreasing and then increasing. Among them, the engine start time of 0.5753 s is lowest at engine starting point E.

This shows that under low-speed and heavy-load conditions and under high-speed and low-load conditions, the engine starting point has a great influence on the engine starting time, and the engine can be started more quickly under medium-speed and medium-load conditions.

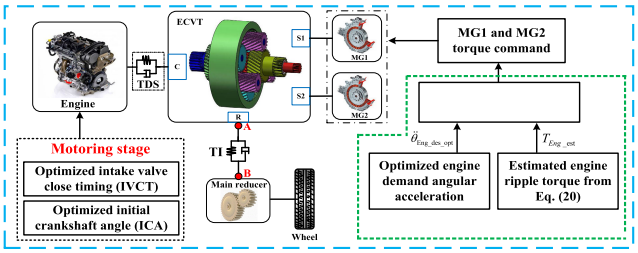

FIGURE 25. Synthesis optimization diagram of engine starting process.

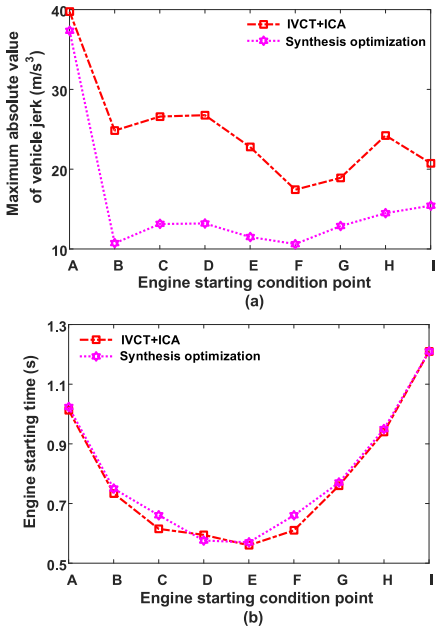

FIGURE 26. Optimization results under different engine starting condition points.

VI. SYNTHESIS OPTIMIZATION OF ENGINE STARTING PROCESS

Based on an analysis of the above factors, as shown in Fig. 25, the engine initial crankshaft angle (160°), intake valve close timing (150°), engine demand angle acceleration (a = 100, b = 200, c = 0.05), and motor torque compensation control are used to synthetically optimize the engine starting process under the basic simulation parameters of the engine starting process in Tables 1 and 2.

Fig. 26 shows the dynamic response results under different engine starting condition points as obtained by the "IVCT + ICA" method and the synthesis optimization method. Note that the "IVCT + ICA" method uses only the engine intake valve close timing (150°) and the engine initial crankshaft angle (160°). It can be seen from Fig. 26(a) that compared with the result of $j_{a-\max}$ obtained by using the BC method in Fig. 24(a), $j_{a-\max}$ has been significantly reduced by using the "IVCT + ICA" method. Compared with the "IVCT + ICA" method, the synthesis optimization method further reduces $j_{a-\max}$.

In addition to point A, $j_{a-\max}$ is reduced to below 20 m/s^3 using the synthesis optimization method. Since the ring demand torque at engine starting point A is relatively large, the torques of the two motors distributed in the engine starting

process are larger than the maximum torque limitations of the two motors, which leads to a greater jerk on the transmission system. In addition, it can be seen from Fig. 26(b) that the difference between the engine starting time obtained by the "IVCT + ICA" method and the synthesis optimization method is not large, but the engine starting time generated by the two methods is significantly smaller than that generated by the BC method in Fig. 24(b).

VII. CONCLUSION

Taking the vehicle jerk and engine starting time as the evaluation indexes of the dynamic response characteristics for a compound power-split HEV, the influencing factors of the dynamic response characteristics in the engine starting process were analyzed comprehensively from the aspects of the engine, battery-motor, and engine starting condition points. The analysis results of the dynamic response characteristics are as follows:

(1) Cold and hot engine starts have little effect on the vehicle jerk, but the cold-start time of the engine is longer than the hot-start time of the engine. Under the engine starting conditions given in this paper, the maximum absolute value of the vehicle jerk and the engine starting time generally increase with an increase in the ratio coefficient of the engine ripple torque, increase in the engine intake manifold pressure, increase of parameter c of the engine demand angular acceleration, decrease in the engine initial crankshaft angle, decrease in the engine intake valve close timing, and decrease in the maximum torque ratio of MG1.

(2) The maximum absolute value of the vehicle jerk and engine starting time will tend toward a constant value with an increase in parameters a and b of the engine demand angular acceleration, increase in the battery charge and discharge power limitations, increase in the maximum torque ratio of MG2, and increase in the motor torque change rate limitations. When the battery temperature and SOC are in a certain range, they do not affect the vehicle jerk or engine starting time. The motor torque compensation control has no obvious effect on the engine starting time, but it can effectively reduce the vehicle jerk.

(3) The engine starting condition points (especially in the low-speed and heavy-load conditions) have a significant impact on the vehicle jerk and engine starting time. In addition, the synthesis optimization method of the engine starting process can effectively reduce the vehicle jerk and engine starting time. This will improve driving comfort during the mode transition process with the engine starting.

REFERENCES

[1] H.-T. Ngo and H.-S. Yan, "Configuration synthesis of parallel hybrid transmissions," *Mechanism Mach. Theory*, vol. 97, pp. 51–71, Mar. 2016.

[2] F. Zhang, X. Hu, R. Langari, and D. Cao, "Energy management strategies of connected HEVs and PHEVs: Recent progress and outlook," *Progr. Energy Combustion Sci.*, vol. 73, pp. 235–256, Jul. 2019.

[3] D. F. Opila, X. Wang, R. McGee, R. B. Gillespie, J. A. Cook, and J. W. Grizzle, "An energy management controller to optimally trade off fuel economy and drivability for hybrid vehicles," *IEEE Trans. Control Syst. Technol.*, vol. 20, no. 6, pp. 1490–1505, Nov. 2012.

[4] W. Wang, R. Song, M. Guo, and S. Liu, "Analysis on compound-split configuration of power-split hybrid electric vehicle," *Mechanism Mach. Theory*, vol. 78, pp. 272–288, Aug. 2014.

[5] G. Jinquan, H. Hongwen, P. Jiankun, and Z. Nana, "A novel MPC-based adaptive energy management strategy in plug-in hybrid electric vehicles," *Energy*, vol. 175, pp. 378–392, May 2019.

[6] Y. Su, M. Hu, L. Su, D. Qin, T. Zhang, and C. Fu, "Dynamic coordinated control during mode transition process for a compound power-split hybrid electric vehicle," *Mech. Syst. Signal Process.*, vol. 107, pp. 221–240, Jul. 2018.

[7] Y. Su, M. Hu, L. Su, D. Qin, and Y. Zhang, "Dynamic coordinated control during mode transition process for a plug-in hybrid electric vehicle," *IEEE Access*, vol. 7, pp. 53891–53908, 2019.

[8] Z. Lei, D. Sun, Y. Liu, D. Qin, Y. Zhang, Y. Yang, and L. Chen, "Analysis and coordinated control of mode transition and shifting for a full hybrid electric vehicle based on dual clutch transmissions," *Mechanism Mach. Theory*, vol. 114, pp. 125–140, Aug. 2017.

[9] F. Zhu, L. Chen, C. Yin, and J. Shu, "Dynamic modelling and systematic control during the mode transition for a multi-mode hybrid electric vehicle," *Proc. Inst. Mech. Eng., D, J. Automobile Eng.*, vol. 227, no. 7, pp. 1007–1023, Jul. 2013.

[10] A. K. Gupta and C. P. Ramanarayanan, "Analysis of circulating power within hybrid electric vehicle transmissions," *Mechanism Mach. Theory*, vol. 64, pp. 131–143, Jun. 2013.

[11] Y. Tong, *Study on the Coordinated Control Issue in Parallel Hybrid Electric System*. Beijing, China: Tsinghua Univ., 2004.

[12] C. Du, F. Yan, Z. Cao, and S. Wu, "Smooth mode-switch control for the powertrain of parallel hybrid electric vehicle," in *Proc. Asia–Pacific Power Energy Eng. Conf.*, Mar. 2009, pp. 1–4.

[13] J. Hong, S. Kim, and B. Min, "Drivability development based on cosimulation of AMESim vehicle model and Simulink HCU model for parallel hybrid electric vehicle," SAE Tech. Paper 2009-01-0725, 2009.

[14] J. Zhang, L. U. Xin, and L. Wang, "A study on the drivability of hybrid electric vehicle," SAE Tech. Paper 2008-01-1572, 2008.

[15] M. Hu, G. Jiang, C. Fu, and D. Qin, "Torque coordinated control in engine starting process for a single-motor hybrid electric vehicle," *Adv. Mech. Eng.*, vol. 9, no. 7, Jul. 2017, Art. no. 168781401770596.

[16] M. Canova, Y. Guezennec, and S. Yurkovich, "On the control of engine Start/Stop dynamics in a hybrid electric vehicle," *J. Dyn. Syst., Meas., Control*, vol. 131, no. 6, Nov. 2009, Art. no. 061005.

[17] M. Canova, K. Sevel, and Y. Guezennec, "Control of the start/stop of a diesel engine in a parallel HEV: Modeling and experiments," in *Proc. ASME Int. Mech. Eng. Congr. Expo.*, 2006, pp. 525–533.

[18] M. Canova, K. Sevel, and Y. Guezennec, "Control of the start/stop of a diesel engine in a parallel HEV with a belted starter/alternator," SAE Tech. Paper 2007-24-0076, 2007.

[19] T. Yoshioka, "Development of noise and vibration reduction technology on hybrid vehicle," *J. Soc. Automot. Eng. Jpn.*, vol. 57, no. 7, pp. 1–7, 2003.

[20] M. Komada and T. Yoshioka, "Noise and vibration reduction technology in new generation hybrid vehicle development," SAE Trans. Tech. Paper 2005-01-2294, 2005, pp. 2648–2655.

[21] T. Yoshioka and H. Sugita, "Noise and vibration reduction technology in hybrid vehicle development," SAE Tech. Paper 2001-01-1415, 2001.

[22] N. Kawabata, M. Komada, and T. Yoshioka, "Noise and vibration reduction technology in the development of hybrid luxury sedan with series/parallel hybrid system," SAE Tech. Paper 2007-01-2232, 2007.

[23] M. L. Kuang, "An investigation of engine start-stop NVH in a power split powertrain hybrid electric vehicle," SAE Tech. Paper 2006-01-1500, 2006.

[24] H.-Y. Hwang, "Minimizing seat track vibration that is caused by the automatic Start/Stop of an engine in a power-split hybrid electric vehicle," *J. Vibrat. Acoust.*, vol. 135, no. 6, Dec. 2013, Art. no. 061007.

[25] J.-S. Chen and H.-Y. Hwang, "Engine automatic start–stop dynamic analysis and vibration reduction for a two-mode hybrid vehicle," *Proc. Inst. Mech. Eng., D, J. Automobile Eng.*, vol. 227, no. 9, pp. 1303–1312, 2013.

[26] X. Tang, D. Zhang, T. Liu, A. Khajepour, H. Yu, and H. Wang, "Research on the energy control of a dual-motor hybrid vehicle during engine start-stop process," *Energy*, vol. 166, pp. 1181–1193, Jan. 2019.

[27] X. Tang, X. Hu, W. Yang, and H. Yu, "Novel torsional vibration modeling and assessment of a power-split hybrid electric vehicle equipped with a dual-mass flywheel," *IEEE Trans. Veh. Technol.*, vol. 67, no. 3, pp. 1990–2000, Mar. 2018.

[28] X. Tang, W. Yang, X. Hu, and D. Zhang, "A novel simplified model for torsional vibration analysis of a series-parallel hybrid electric vehicle," *Mech. Syst. Signal Process.*, vol. 85, pp. 329–338, Feb. 2017.

[29] Xiaohua Zeng, H. Cui, D. Song, N. Yang, T. Liu, H. Chen, Y. Wang, and Y. Lei, "Jerk analysis of a power-split hybrid electric vehicle based on a data-driven vehicle dynamics model," *Energies*, vol. 11, no. 6, p. 1537, 2018.

[30] X. Zeng, N. Yang, J. Wang, D. Song, N. Zhang, M. Shang, and J. Liu, "Predictive-model-based dynamic coordination control strategy for power-split hybrid electric bus," *Mech. Syst. Signal Process.*, vols. 60–61, pp. 785–798, Aug. 2015.
[31] D. Liu, J. Zhang, D. Zhang, G. Liu, and H. Yu, "Experimental and numerical analysis of the seat track vibrations caused by engine starts in a power-split hybrid electric vehicle," *Proc. Inst. Mech. Eng., D, J. Automobile Eng.*, vol. 231, no. 3, pp. 395–404, Feb. 2017.
[32] D. Liu, H. Yu, and J. Zhang, "Multibody dynamics analysis for the coupled vibrations of a power split hybrid electric vehicle during the engine start transition," *Proc. Inst. Mech. Eng., K, J. Multi-body Dyn.*, vol. 230, no. 4, pp. 527–540, Dec. 2016.
[33] C. Wang, Z. Zhao, T. Zhang, and M. Li, "Mode transition coordinated control for a compound power-split hybrid car," *Mech. Syst. Signal Process.*, vol. 87, pp. 192–205, Mar. 2017.
[34] H. L. Benford and M. B. Leising, "The lever analogy: A new tool in transmission analysis," in *Proc. SAE Trans.*, 1981, pp. 429-437. [Online]. Available: https://www.sae.org/publications/technical-papers/content/810102/
[35] L. Zhou, *Study the Internal Combustion Engine*. Machinery Industry Press, 2011. [Online]. Available: https://xueshu.baidu.com/usercenter/paper/show?paperid=1de0154d1eb0be0e34a35417e763255c&site=xueshu_se
[36] L. Guzela and C. H. Wendell, *Introduction to Modeling and Control of Internal Combustion Engine*. Mechanical Industry Press, 2016. [Online]. Available: https://books.google.com.hk/books?hl=en&lr=&id=BsN9-v0esd8C&oi=fnd&pg=PR2&dq=Introduction+to+Modeling+and+Control+of+Internal+Combustion+Engine&ots=z4efaQjTU6&sig=tPNlX9Ket1vHjrN7y_2_8BonKI8&redir_esc=y#v=onepage&q=Introduction%20to%20Modeling%20and%20Control%20of%20Internal%20Combustion%20Engine&f=false
[37] D. Yuan, Y. Xu, and X. Li, *Variable Frequency System of Permanent Magnet Synchronous Motor and Control*. Mechanical Industry Press, 2015. [Online]. Available: https://xueshu.baidu.com/usercenter/paper/show?paperid=d080fadc092be6395e3d6a50ec54a8c3&site=xueshu_se&hitarticle=1
[38] Y. Su, M. Hu, and L. Su, "Study on dynamic characteristics of electromechanical coupling in mode switching process of multi-power transmission system considering internal and external excitation," in *Proc. JSME Int. Conf. Motion Power Transmiss.*, 2017, pp. 545–550.
[39] X. Wei, P. Pisu, and G. Rizzoni, "Dynamic modeling of a hybrid electric drivetrain for fuel economy, performance and driveability evaluations," in *Proc. ASME Int. Mech. Eng. Congr. Expo.*, 2003, pp. 443–450.
[40] M. Mueller, "Engine stop position estimation," *SAE Int. J. Engines*, vol. 5, no. 2, pp. 602–607, 2012.

YANZHAO SU was born in Zhengzhou, Henan, China. He is currently pursuing the Ph.D. degree in vehicle engineering with Chongqing University, Chongqing, China.

He is also a joint Ph.D. Student with the University of Michigan-Dearborn, USA. He participates in the National Natural Science Foundation of China and the National Key Research and Development Project. He has published several articles on hybrid cars. He has applied for several national invention patents on the configurations of hybrid electric vehicles. His research interest includes design and analysis and control of power transmission systems.

LING SU was born in Chongqing, China. He received the B.S., M.S., and Ph.D. degrees in mechanical engineering from Xi'an Jiaotong University, in 1998, 2001, and 2005, respectively.

He is currently a Senior Engineer of new energy vehicle with Chongqing Changan Automobile Company Ltd., and the Deputy General Manager of Changan New Energy Automobile Company. He has over 14 years of extensive experience in the field of new energy vehicle, since 2005. He has been leading or participated in over ten research projects. He has published more than ten academic articles. He is the owner of over 35 invention patents. He has received many honours, such as the China Auto Industry Science and Technology Award, the Chongqing Technology Invention Award, and the Chongqing Science and Technology Progress Award.

MINGHUI HU (Member, IEEE) was born in Xi'an, China. He received the B.S., M.S., and Ph.D. degrees in mechanical engineering from Chongqing University, in 1998, 2003, and 2007, respectively.

He has been serving as a Professor with the School of Automotive Engineering, Chongqing University, since 2017. He has over 17 years of extensive experience in the field of vehicle power transmission systems, since 2000. He has been leading or participated in over 70 research projects. He has published more than 90 academic articles which are published in prestigious journals. He is the owner of over 30 invention patents. He was awarded the Local Government Prize and the China South Industries Group Corporation Prize for his research achievements in the field of vehicle powertrain systems.

DATONG QIN (Member, IEEE) was born in Chongqing, China, in November 1956. He received the B.S., M.S., and Ph.D. degrees in mechanical engineering from Chongqing University, in 1982, 1984, and 1993, respectively.

He was a Visiting Scholar with the Department of Precision Engineering, Tohoku University, Japan, from 1989 to 1991. He was the Deputy Director of the SKLMT of China, from 1995 to 1997, and the Director, from 1997 to 2008. Since 2009, he has been the Vice Dean (part time) of the Graduate School of Chongqing University. He was appointed by Ministry of Education of China as the Changjiang Chair Professor, in 2005. His fields of research include powertrain systems for conventional vehicles and hybrid electric vehicles, gearing theory and gearing transmission systems. He has published more than two hundreds of academic articles, which have been published in national and international journals or presented at national and international conferences. He is the owner of more than twenty invention patents. He was awarded two national prize by Central Government of China and 11 prizes by Ministry of Education or Local Government for his research achievements in the areas of powertrain systems of vehicles and gear transmission.

CHUNYUN FU (Member, IEEE) received the bachelor's degree from Chongqing University, China, in 2010, and the Ph.D. degree from RMIT University, Australia, in 2015. He is currently a Lecturer with the School of Automotive Engineering, Chongqing University. His main research interests include electric vehicles and autonomous vehicles.

HAISHENG YU received the Ph.D. degree in mechanical engineering from Shanghai Jiao Tong University, Shanghai, China, in 2012. He is currently the Deputy Technology Department Director of Corun Hybrid System Technology Company Ltd., Changsha, China. His research interests include mechatronics systems and control theory, and the hybrid-drive transmission. He has more than ten years of work experience in the HEV research field, especially in the control strategy design of the parallel HEV and series–parallel HEV.